Reconfinement and Loss of Stability in Jets from Active Galactic Nuclei

Konstantinos N. Gourgouliatos[*†] and Serguei S. Komissarov[‡]

February 19, 2018

Jets powered by active galactic nuclei appear impressively stable compared with their terrestrial and laboratory counterparts they can be traced from their origin to distances exceeding their injection radius by up to a billion times.[1,2] However, some less energetic jets get disrupted and lose their coherence on the scale of their host galaxy.[1,3] Quite remarkably, on the same scale, these jets are expected to become confined by the thermal pressure of the intra-galactic gas.[2] Motivated by these observations, we have started a systematic study of active galactic nuclei jets undergoing reconfinement via computer simulations. Here, we show that in the case of unmagnetized relativistic jets, the reconfinement is accompanied by the development of an instability and transition to a turbulent state. During their initial growth, the perturbations have a highly organized streamwise-oriented structure, indicating that it is not the KelvinHelmholtz instability, the instability which has been the main focus of the jet stability studies so far.[4,5] Instead, it is closely related to the centrifugal instability.[6] This instability is likely to be behind the division of active galactic nuclei jets into two morphological types in the Fanaroff–Riley classification.[7]

It has been proposed[2] that the extraordinary surviving ability of active galactic nuclei (AGN) jets is due to the fact that outside of the jet engine they are no longer confined but expand freely in the lowpressure interstellar environment. This leads to a loss of causal connectivity across the jet, which suppresses any global instability. Yet, such a free expansion does not last forever as the thermal pressure of freely expanding jets rapidly decreases. Eventually, it becomes lower than the external pressure and the jets become confined again. The reconfinement involves a strong stationary (or quasi-stationary) shock that communicates the external pressure to the jet interior. Once it reaches the jet axis at the reconfinement point (RP), the process of reconfinement is completed. Downstream of the RP, causal connectivity across the jet is restored and this is where it may become vulnerable to global instabilities.

[*]Department of Applied Mathematics, University of Leeds, Leeds, LS2 9JT, UK

[†]Department of Mathematical Sciences, Durham University, Mountjoy Centre, Stockton Rd, Durham DH1 3LE, UK, Konstantinos.Gourgouliatos@durham.ac.uk

[‡]Department of Applied Mathematics, University of Leeds, Leeds, LS2 9JT, UK, s.s.komissarov@leeds.ac.uk

So far, two types of instability have been identified as important in the dynamics of AGN jets, the KelvinHelmholtz instability (KHI)[4,5] and the magnetic current-driven instabilities,[8,9] which have been explored in detail in numerous studies. Both linear analysis and numerical studies of jet instabilities have focused on the cylindrical geometry of the background flow. The geometry of reconfined jets is more complicated, with curved streamlines even for non-rotating flows.

Motivated by the idea of causal connectivity, we performed computer simulations of relativistic jets undergoing reconfinement. As a first step, only unmagnetised flows were considered. Following the standard route of stability analysis, we started the investigation of each particular jet model by constructing its steady-state solution. To this aim, we used the approach from ref.[10] This solution was then projected onto a two-dimensional (2D) and three-dimensional (3D) computational grid to serve as an initial state for timedependent simulations.

We considered two different models of the external gas. The first describes the interstellar gas of elliptical galaxies.[11] It is isothermal with flat density distribution up to the galactic core radius $r_c = 1$ kpc followed by a decline as $r^{-1.25}$. Reflecting the observations, this gas is significantly heavier than the jet gas. The second model is designed to simulate the conditions inside the radio lobes of FR-II jets. In this model, the external gas is uniform and significantly lighter than the jet.

At the nozzle, the steady-state solution corresponds to a highly supersonic conical jet emerging from the centre of a galaxy. Its Lorentz factor (Γ) is maximum at the axis and decreases towards the edge of the jet, while its density and pressure are uniform. The key problem parameter is the jet kinetic power, which determines the position of the RP.[2] We ran several models covering a wide range of the RP position compared with the galactic core radius. The nozzle location was selected to allow substantial initial expansion of the jet before its reconfinement. The size of the computational domain was at least twice the distance from the nozzle to the RP.

When the gas density and velocity profiles were too steep at the jet interface, the time-dependent solution was corrupted by numerical heating, which drove strong shocks into the jet and into the external gas right at the start of the simulations. To prevent this from happening, we introduced a boundary layer where the density changed gradually. With such a modification, our axisymmetric 2D solutions eventually relaxed to a steady state that was only slightly different from the initial one, indicating its stability. The stability of such axisymmetric models was reported earlier by another group.[12]

In stark contrast with these axisymmetric solutions, our 3D jets exhibit a completely different evolutiontheir reconfinement is accompanied by a loss of stability and a quick transition to a fully turbulent state. This is illustrated in Fig. 1, which confronts the 2D and 3D solutions for a jet propagating through a galactic corona (model C1 in Supplementary Table 1). One can see that the instability already develops before the RP in the shocked outer layer of the still expanding jet, but then it takes hold over the whole of the jet once the reconfinement shock reaches the jet axis. Such a behaviour is seen in all our models. The turbulence is very strong and leads to substantial heating of the jet plasma downstream of the reconfinement shock. Its pressure rises well above that of the steady-state model and this drives a shock into the cold interstellar plasma as well as forcing the RP to move towards the jet origin.

The structure of perturbations before the transition to turbulence can give away the nature of instability. In our case, the axial slices of the solution do not show the characteristic eddies of KHI, whereas the transverse jet structure reveals prominent features reminiscent more of the RayleighTaylor instability (RTI). 3D rendering of the solution shows that these features are in fact stretched along the streamlines of the background flow (see Fig. 2).

As in rotating fluids, the plasma of reconfined jets moves along curved streamlines and hence experiences a centrifugal force. This suggests that our instability could be related to instabilities found in rotating flows. In particular, it is well known that rotating flows of an incompressible fluid of uniform density, rotating with angular velocity Ω, experience the so-called centrifugal instability (CFI) when the Rayleigh[6] discriminant $\Psi = \Omega^2 R^4$ decreases with distance (R) from the centre of rotation. This condition is always satisfied when the rotation is brought to a halt at a given distance, which is the case in our jet problem. This instability is known to produce stream-oriented features like the Taylor vortices in the Couette flow and the Grtler vortices in flows over concave surfaces.[13] These vortices spin about the streamlines of the background flow, which in the context of our problem implies a nonaxisymmetric motion and hence explains why the instability did not show up in the 2D simulations. The condition for the development of the CFI in an axially symmetric relativistic flow, where the assumptions of uniform density and incompressibility have been relaxed, becomes[14]

$$\frac{d \ln \Psi}{d \ln R} < M^2 \tag{1}$$

where $\Psi = \Gamma^2 w \Omega^2 R^4$, Γ is the Lorentz factor, w is the relativistic enthalpy and $M = (\Gamma \Omega R)/(\Gamma_a a)$ is the relativistic Mach number where a is the speed of sound and Γ_a is the corresponding Lorentz factor. This condition is trivially satisfied in the systems studied here, where a curved flow is confined by an external medium at rest.

It has been argued[15] that the spatial oscillations of reconfined jets are somewhat similar to the oscillations of initially over-pressured infinite cylindrical jets with translational symmetry. These researchers carried out 2D simulations of cylindrical flows and discovered that they suffered RTI provided the external gas was relatively light.[15] However, their configuration was different. In their approach, not only the jet but also the external gas participates in the sideways expansion and the centrifugal force vanishes. In our simulations, the instability develops independent of the external gas density, implying that it is not RTI.

Our simulations show that in contrast with idealised cylindrical flows, in more realistic models of AGN jets one has to consider the competition between KHI and CFI. The fastest growing KHI modes in supersonic cylindrical jets are the reflection body modes for which the jet serves as an acoustic waveguide.[17] The complicated non-cylindrical structure of reconfined jets may prevent them from supporting such modes. The growth rate of CFI modes has to depend on the curvature of the jet streamlines and hence the jet half-opening angle θ_j. The value of θ_j used in most of our models appears a bit high compared with the observations, but θ_j used in the model C5 is similar to that measured for the jets of Cygnus A.[18] In this model, CFI still dominates over KHI.

AGN jets are magnetized and the magnetic field is believed to play a key role in their dynamics near the central engine. These jets are likely to be Poynting-dominated

at the start but, even for the relatively slow ideal collimationacceleration mechanism, the process of conversion of magnetic energy into the kinetic energy of bulk motion is expected to be completed already at sub-parsec scales.[19] Hence, on the kpc scales considered in our study, the magnetic field is likely to be relatively weak. However, it may still affect the development of non-magnetic instabilities and introduce new ones.[19] Simulations of magnetized jets is the next step of our study.

The position of the RP point depends on the jet power. For the typical distribution of the galactic gas, it varies from ~ 50 pc for the weakest AGN jets (of power $L = 10^{42}$ erg s^{-1}) to ~ 50 kpc for the most powerful ones ($L = 10^{47}$ erg s^{-1}).[2] This agrees with the observed wide range of flaring distances for AGN jets.[3] However, for the high end of the power distribution, our approach becomes less justified. It is unlikely that at such large distances the adopted model of the external gas distribution still holds. Moreover, the longest jets appear to be shielded from the external medium by light cocoons.

On the large scale, AGN jets inflate bubbles of radio-emitting plasma, the so-called radio lobes. In the less powerful FR-I sources, the lobe brightness peaks within the inner half of their extent, whereas in the more powerful FR-II sources, this happens within the outer half, often close to the very edge.[7] FR-I jets appear to be disrupted and dissolve into the lobes. FR-II jets can often be traced all the way to the most distant parts of the radio lobes, where they terminate at bright hot spots. Our results explain the FR-I jets as those destroyed by instabilities triggered when they are reconfined by the pressure of the intra-galactic gas.

The basic dynamic theory of FR-II jets predicts that they are reconfined by the bubbles thermal pressure instead. This occurs well before the jets terminate at the leading hot spots[21,22] and hence they are expected to experience global instabilities as well. However, in contrast with FR-I jets, their surrounding is much lighter, which has important implications for the overall jet evolution. Indeed, our simulations of jets reconfined by light gas also show rapid onset of the centrifugal instability at RP, after which the jets still become turbulent but they do not flare and remain rather well preserved (see Figs. 3 and 4). Most likely, this reflects the differences in the turbulent mass entrainment.[23,24] When the external gas is light, the rate of mass entrainment is lower and so is its effect on the jet flow. This may explain why FR-I jets turn sub-relativistic, whereas the FR-II jets show signatures of relativistic motion all the way up to the leading hot spots.[23,24]

Many AGN jets can be traced to much smaller distances compared with the kpc reconfinement scale discussed here. They usually display a knotty structure, which is often considered as an indication of an unsteady central engine. Most of these knots are seen to be moving away from the centre of the parent galaxy. However, a few of them appear to be more or less stationary and these have been associated with quasi-stationary shocks.[26,27] Since the jets survive well beyond these shocks, they should differ from the reconfinement shocks considered here. Instead, they could be recollimation shocks, which never reach the jet axis, leaving it causally disconnected and globally stable.[28] Another option involves non-destructive jet interaction with clouds of interstellar gas or even stellar winds from clusters of young stars.[24,29]

In a small fraction of AGN, one extended radio lobe has the FR-I morphology, while another has the FR-II morphology.[30] It has been argued that the existence of such hybrid sources supports the idea that the source morphology is not dictated by the

specifics of AGN, which is the same for both lobes, but by the jet interaction with the external gas, which may have a highly anisotropic distribution. Our study clarifies the nature of this interaction.

In summary, our results provide strong support to the ideas that: (1) the long-term stability of AGN jets is due to their rapid expansion; and (2) the FR-division of radio sources is connected to the eventual termination of this expansion and onset of instabilities. Unexpectedly, we also find that the transition from the laminar to the fully turbulent flow occurs about the PR and it is very sharp compared with what is normally seen in laboratory supersonic jets. This sharp transition may explain the observed geometric and brightness flaring of FR-I jets on the kiloparsec scale.[3] According to the observations, FR-I jets also show significant deceleration at the flaring point, after which the flow often becomes slower at its edges than it is on-axis. This is exactly what occurs in our 3D models.

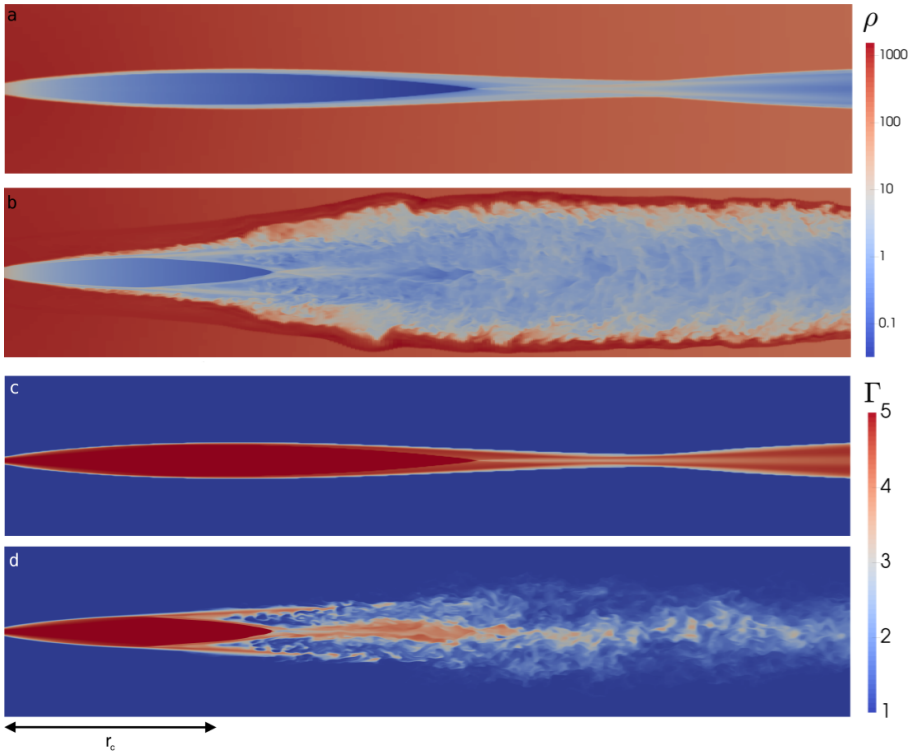

Fig. 1: **Jet density (ρ, panels a and b) and Lorentz factor (Γ panels c and d), for the model C1, corresponding to an FR-I jet making its way through a galactic corona. a–d**, The $y = 0$ section of the jet, containing the axis of the jet, is shown for ρ (**a**) and Γ (**c**) in the steady state solution and ρ (**b**) and Γ (**d**) in the final 3D solution at $t = 32.6$ kyr. The origin of coordinates is located at the galactic centre and the z axis runs along the jet. The radius of the core of the galaxy is $r_c = 1$ kpc. The density is expressed in arbitrary units and this applies for all subsequent figures (please refer to Supplementary Table 1 where the details of the run are presented). When analysing such plots, one has to remember that the 3D flows are no longer axisymmetric and significant structure may exist in the azimuthal direction. The 3D solution has a recessed RP compared with the steady-state one, which is a general property of all our models. Downstream of the RP, the flow is highly turbulent. The Lorentz factor distribution looks narrower compared with the density distribution, indicating that the jet has developed a fast-spine-slow-sheath structure in the turbulent zone. The dense shell surrounding the jet is a shock-compressed external gas. The dissipation of jet kinetic energy in the turbulent zone causes its heating and sideways expansion, which drives a quasi-cylindrical shock through the cold gas of the galactic corona. Longer runs are required to reach the stationary in the statistical sense phase that must follow this initial expansion.

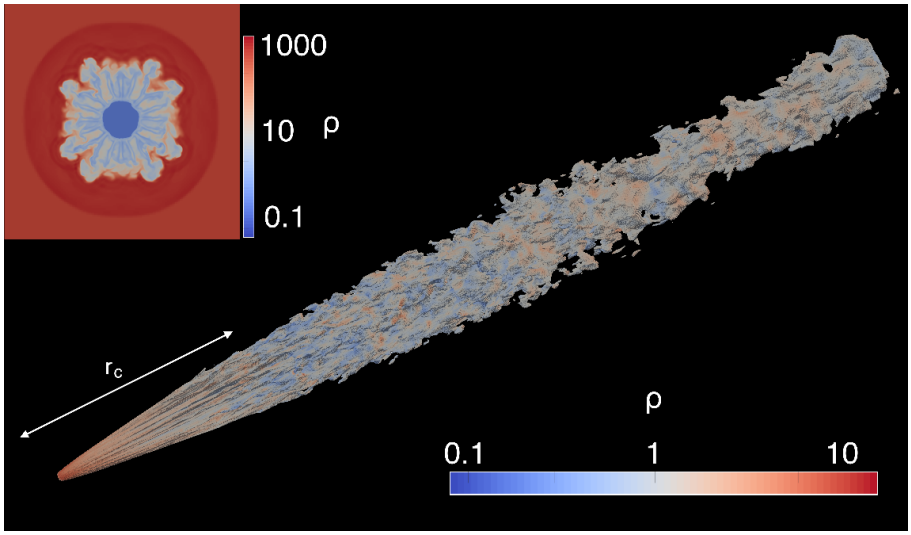

Fig. 2: **3D rendering of model C1 at the end of the run t = 32.6 kyr.** The insert shows the corresponding density distribution in the cross-section $z \approx r_c$, just before the flow turns turbulent. Based on this inserted image alone, one may conclude that we are dealing with the RTI, but the 3D rendering shows that the perturbations are stretched along the streamlines of the background flow and form a rather regular pattern in the first quarter of the jet length. Such patterns have never been seen before in laboratory jets or jet simulations, but are known in other flows. The most familiar examples are the Taylor and Görtler vortices, which are associated with the CFI.

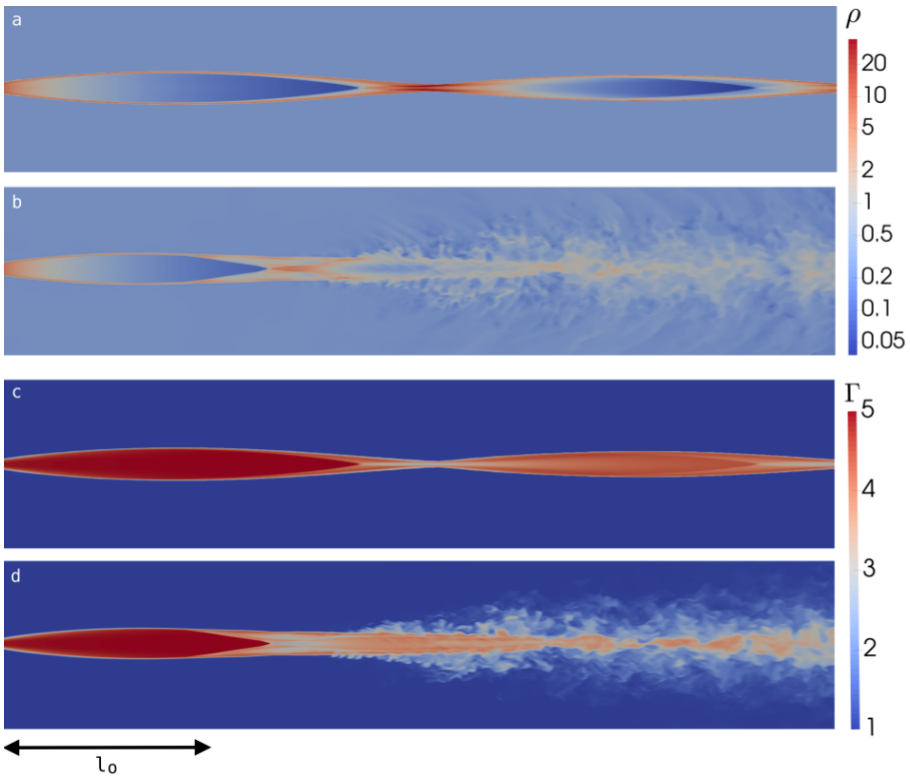

Fig. 3: **Jet density (ρ) and Lorentz factor (Γ) for the model U2, representative of an FR-II jet. a – d,** Solutions at the beginning of the run for ρ (**a**) and ρ (**c**) and at the end of the run ρ (**b**) and Γ (**d**) (t = 32.6kyr), with l_0 = 1 kpc, for a section as in Fig. 1. Similar to the C1 case, the jet turns turbulent on the reconfinement scale but it appears less disrupted, with a fast spine surviving all the way up to the right boundary of the computational domain.

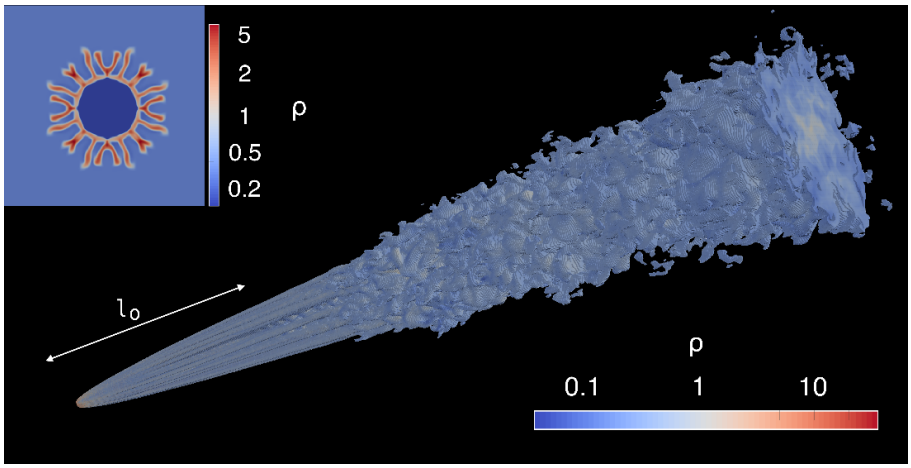

Fig. 4: **3D rendering of model U2 at the end of the run t = 32.6 kyr.** The insert shows the corresponding density distribution in the cross-section $z \approx l_0$, just before the flow turns turbulent. The jet appears to be wider compared with the C1 jet in Fig. 2, but this is not significant and conveys more about the properties of the numerical diffusion than the actual jet dynamics.

Methods

Below, we present the setup used for the simulations described in this study. Throughout this work, we used the AMRVAC code as described in refs,[31,32] integrating the equations of relativistic hydrodynamics

$$\partial_t (\rho\Gamma) + \nabla_i \left(\rho\Gamma v^i\right) = 0\,, \tag{2}$$

$$\partial_t \left(\rho h\Gamma^2 - p\right) + \nabla_i \left(\rho h\Gamma^2 v^i\right) = S_0\,, \tag{3}$$

$$\partial_t \left(\rho h\Gamma^2 v_j\right) + \nabla_i \left(\rho h\Gamma^2 v^i v_j + p\delta^i_j\right) = S_j\,, \tag{4}$$

where Γ is the Lorentz factor, v is the velocity, ρ is the rest mass density in the fluid frame, p is the pressure and $h = 1 + \gamma/(\gamma - 1)\,(p/\rho)$ is the specific enthalpy of ideal gas. S_0 and S_j are the source terms introduced to keep the external gas in equilibrium (see below). In the simulations, $\gamma = 4/3$. We used the HLLC Riemann solver,[33] Koren flux limiter and two-step RungeKutta method for time integration. To implement this, we used the built-in routines of the code.

Steady-state Solutions. Steady-state solutions. To study the stability of a steady-state solution describing a jet reconfined by the thermal pressure of the external gas, we needed to find this solution first. To this aim, we used the approach described in ref.,[10] where an approximate steady-state solution for an axisymmetric jet was found by solving a corresponding one-dimensional time-dependent problem in cylindrical geometry. Such solutions are sufficiently accurate provided the jet is narrow and highly

relativistic, with the jet speed $v \approx c$. In these time-dependent simulations, the initial conditions describe the parameters at the nozzle of the steady-state problem. Here, we assume the initial jet Lorentz factor

$$\Gamma = \begin{cases} \Gamma_0 \left[1 - \left(\frac{R}{R_j}\right)^4\right] + \left(\frac{R}{R_j}\right)^4 , & R \leq R_j \\ 1 , & R > R_j \end{cases} \tag{5}$$

where R is the cylindrical radius, and the velocity vector

$$(v_R, v_\phi, v_z) = v\,(\sin\theta, 0, \cos\theta) \tag{6}$$

where v is the speed corresponding to Γ, $\theta = \arctan(R/z_0)$ and z_0 is the nozzles distance from the jet origin. The z direction is aligned with the jet axis and hence this velocity distribution corresponds to a conical jet emerging from the origin. In the simulations, we assumed that $z_0 = 0.1 r_c$ and $R_j = 0.02 r_c$, where r_c is the galactic core radius. These give the half-opening angle $\theta_j = 0.2$. We also carried out a simulation with an opening angle of $\theta = 0.1$, $\Gamma_0 = 5$ and $L_{j,44} = 2$ (see run C5 in Supplementary Table 1). Although the opening angles of AGN jets are somewhat smaller, the position of the RP only weakly depends on the opening angle for as long as $\theta_j \ll 1$. Our choice of θ_j is dictated by the need to keep the computational time of 3D simulations manageable. Both the initial density and pressure distributions are uniform across the nozzle. The steady-state solution is reconstructed from the time-dependent one via the substitution $z = z_0 + ct.$. We consider an external pressure that depends on the distance from the origin so that $p_e = p_e(r)$ and we use the substitution:

$$r(t)^2 = R^2 + z(t)^2 .$$

so that the pressure becomes a function of the cylindrical distance and time.

We identify the external gas using the level set method[34] with a passive tracer τ satisfying the equation:

$$\frac{\partial\,(\Gamma\rho\tau)}{\partial t} + \nabla_i \left(\Gamma\rho\tau v^i\right) = 0 . \tag{7}$$

The tracer is initialised via

$$\tau = \frac{1}{2}\left[1 - \tanh\left(\frac{R - R_j}{w}\right)\right] , \tag{8}$$

with $w = 0.05 R_j$. The transition from the jet to the external medium occurs when the passive tracer value drops below the cut-off value $\tau_b = 0.5$. As we integrate forward in time, we reset the value of the pressure to $p_e(r(t))$ for every time step for cells with $\tau < \tau_b$.

Coronas of elliptical galaxies are modelled as hydrostatic isothermal atmospheres with the density distribution

Coronas of elliptical galaxies are modelled as hydrostatic isothermal atmospheres with the density distribution

$$\rho_e(r) = \rho_{e,0}\left[1 + \frac{r^2}{r_c^2}\right]^{-a/2} , \tag{9}$$

where r_c is the radius of the galactic core. For all models, we use $r_c = 1$ kpc and $a = 1.25$–the typical values for giant elliptical galaxies. Since the initial opening angle of our simulated jets is higher than that of AGN jets, the jet density is lower. Because the jet-to-external-gas-density ratio is considered as one of the key parameters in the jet dynamics, we opted to lower the external gas density by the same factor. Since the position of the RP is determined by the external pressure,[2] the latter was kept unchanged with the core pressure $p_{e,0} = 3 \times 10^{-10}\mathrm{dyn\,cm^{-2}}$, leading to a higher external temperature. The parameters of jet models covered in this study are given in Supplementary Table 1.

As a guide, we use the analytical model[2] to estimate the position of the RP and hence decide on the size of the computational domain and the integration time. At the left boundary ($R = 0$), the boundary conditions are dictated by the geometry, which is symmetric for the scalar quantities (density, pressure and passive tracer) and the axial component of the velocity and antisymmetric for the radial and azimuthal velocity component. At the right boundary, we impose the zero-gradient conditions. Our convergency study shows that at the nozzle the jet radius has to be resolved by at least 20 cells.

2D Simulations. The 2D simulations are intended to test the jet stability to axisymmetric perturbations. The size of the cylindrical computational domain $(0, R_d) \times (z_0, z_1)$ is decided based on the parameters of the steady-state solution. The initial solution is set via projecting the steady-state solution onto the 2D cylindrical grid. At $R = 0$, the boundary conditions are dictated by axisymmetry. At the external boundary $R = R_d$, we use the zero-gradient conditions. At $z = z_0$, the parameters of the ghost cells are fixed to those of the external gas for $R > R_j$, whereas for $R < R_j$, we use the parameters of the steady-state jet instead. Finally, the zero gradient conditions are employed at $z = z_1$. In the simulations, we use a single uniform grid with a resolution of 20 cells per jet radius at the nozzle. The cell shape is $\Delta R = 0.2\Delta z$. This is exactly the same shape and resolution as those of the finest grid in our 3D runs.

Preliminary test runs with such a setup revealed very strong numerical dissipation at the jet boundary leading to rapid corruption of the initial solution. We have found that this can be prevented by replacing the density discontinuity at the jet boundary with a smooth transition layer with a tanh-profile of thickness $\Delta R = 0.1R_j$. The same approach is used in the 3D simulations.

When the external gas distribution corresponds to that of galactic coronas, we need to make sure that it does not evolve unless it is perturbed by the jet. To this aim, we have implemented the Newtonian gravity model.[35] This is achieved using the source term

$$S_0 = aH\rho\frac{v^i r_i}{r_c^2 + r^2} \tag{10}$$

into the energy equation and

$$S_j = aH\rho\frac{r_j}{r_c^2 + r^2} \tag{11}$$

into the momentum equation, where $H = p_{e,0}/\rho_{e,0}$.

3D Simulation. In our 3D simulations, we use the Cartesian domain $(-R_d, R_d) \times (-R_d, R_d) \times (z_0, z_1)$. R_d is set to a few times the largest jet radius in the steady-state solution and z_1 to about twice the distance to RP in this solution. The initial 3D solution is prepared in the same fashion as in the 2D simulations described above. At $z = z_0$ and $z = z_1$ we use the same boundary conditions as in the 2D simulations and at the remaining boundaries we enforce the zero-gradient conditions. As in the 2D simulations, Newtonian gravity is introduced to keep the unperturbed external gas in hydrostatic equilibrium.

As a rule, we perturb the initial solution by multiplying the jet density by $1 + 10^{-2} \cos\phi$ and its pressure by $1 + 10^{-2} \sin\phi$, where $1 + 10^{-2} \sin\phi$. If such perturbations are not introduced, the growing perturbations are dominated by the mode with the azimuthal number $m = 4$, which is aligned with the Cartresian grid, indicating that the perturbations come from the discretisation errors. However, the overall evolution does not change much.

In the 3D runs, we benefit from the adaptive mesh capabilities of the AMRVAC code. We introduced four levels of adaptive mesh refinement and used the Lohner refinement criterion[36] based on the behaviour of the Lorentz factor. The resolution of the base level is set to 100^3, corresponding to 20 cells per nozzle radius at the finest grid. The cell shape is $\Delta x = \Delta y = 0.2\Delta z$; we have experimented with various aspect ratios and conclude that for this choice the results are sufficiently close to those with the aspect ratio of unity.

Data Availability Statement

The data that support the plots within the paper and other findings are available from the corresponding author up reasonable request.

Received: 9 June 2017; Accepted: 10 November 2017;

References

[1] Begelman, M. C., Blandford, R. D. & Rees, M. J. Theory of extragalactic radio sources. *Rev. Mod. Phys.* **56**, 255–351 (1984).

[2] Porth, O. & Komissarov, S. S. Causality and stability of cosmic jets. *Mon. Not. Roy. Astron. Soc.* **452**, 1089–1104 (2015).

[3] Laing, R. A. & Bridle, A. H. Systematic properties of decelerating relativistic jets in low-luminosity radio galaxies. *Mon. Not. Roy. Astron. Soc.* **437**, 3405–3441 (2014).

[4] Birkinshaw, M. *The stability of jets*. Cambridge University Press, Cambridge, UK, (1991).

[5] Bodo, G., Mignone, A. & Rosner, R. Kelvin-Helmholtz instability for relativistic fluids. *Phys. Rev. E.* **70**, 036304 (2004).

[6] Rayleigh, L. On the Dynamics of Revolving Fluids. *Proc. of the Royal Soc. A* **93**, 148–154 (1917).

[7] Fanaroff, B. L. & Riley, J. M. The morphology of extragalactic radio sources of high and low luminosity. *Mon. Not. Roy. Astron. Soc.* **167**, 31P–36P (1974).

[8] Bateman, G. *MHD instabilities*. MIT Press, Cambridge, Massachusetts, (1978).

[9] Appl, S., Lery, T. & Baty, H. Current-driven instabilities in astrophysical jets. Linear analysis. *Astron. Astrophys.* **355**, 818–828 (2000).

[10] Komissarov, S. S., Porth, O. & Lyutikov, M. Stationary relativistic jets. *Comput. Astrophys. and Cosmology* **2**, 9 (2015).

[11] Mathews, W. G. & Brighenti, F. Hot Gas in and around Elliptical Galaxies. *Ann. Rev. Astron. Astroph.* **41**, 191–239 (2003).

[12] Martí, J. M., Perucho, M. & Gómez, J. L. The Internal Structure of overpressured, Magnetized, Relativistic Jets. *Astrophys. J.* **831**, 163 (2016).

[13] Saric, W. S. Gurtler vortices. *Annu. Rev. of Fluid Mech.* **26**, 379–409 (1994).

[14] Gourgouliatos, K. N. & Komissarov, S. S. Relativistic Centrifugal Instability. *ArXiv e-prints* (2017). `arXiv:1710.01345`.

[15] Matsumoto, J. & Masada, Y. Two-dimensional Numerical Study for Rayleigh-Taylor and Richtmyer-Meshkov Instabilities in Relativistic Jets. *Astrophys. J. Lett.* **772**, L1 (2013).

[16] Matsumoto, J., Aloy, M. A. & Perucho, M. Linear Theory of the Rayleigh-Taylor Instability at a Discontinuous Surface of a Relativistic Flow. *Mon. Not. Roy. Astron. Soc.* **472**, 1421–1431 (2017).

[17] Payne, D. G. & Cohn, H. The stability of confined radio jets - The role of reflection modes. *Astrophys. J.* **291**, 655–667 (1985).

[18] Boccardi, B. *et al.* The stratified two-sided jet of Cygnus A. Acceleration and collimation. *Astron. Astrophys.* **585**, A33 (2016).

[19] Komissarov, S. S., Barkov, M. V., Vlahakis, N. & Königl, A. Magnetic acceleration of relativistic active galactic nucleus jets. *Mon. Not. Roy. Astron. Soc.* **380**, 51–70 (2007).

[20] Tchekhovskoy, A. & Bromberg, O. Three-dimensional relativistic MHD simulations of active galactic nuclei jets: magnetic kink instability and Fanaroff-Riley dichotomy. *Mon. Not. Roy. Astron. Soc.* **461**, L46–L50 (2016).

[21] Falle, S. A. E. G. Self-similar jets. *Mon. Not. Roy. Astron. Soc.* **250**, 581–596 (1991).

[22] Komissarov, S. S. & Falle, S. A. E. G. The large-scale structure of FR-II radio sources. *Mon. Not. Roy. Astron. Soc.* **297**, 1087–1108 (1998).

[23] Bicknell, G. V. A model for the surface brightness of a turbulent low Mach number jet. I - Theoretical development and application to 3C 31. *Astrophys. J.* **286**, 68–87 (1984).

[24] Komissarov, S. S. Mass-Loaded Relativistic Jets. *Mon. Not. Roy. Astron. Soc.* **269**, 394 (1994).

[25] Giovannini, G., Cotton, W. D., Feretti, L., Lara, L. & Venturi, T. VLBI Observations of a Complete Sample of Radio Galaxies: 10 Years Later. *Astrophys. J.* **552**, 508–526 (2001).

[26] Cohen, M. H. *et al.* Studies of the Jet in Bl Lacertae. I. Recollimation Shock and Moving Emission Features. *Astrophys. J.* **787**, 151 (2014).

[27] Jorstad, S. G. *et al.* Kinematics of Parsec-scale Jets of Gamma-Ray Blazars at 43 GHz within the VLBA-BU-BLAZAR Program. *Astrophys. J.* **846**, 98 (2017).

[28] Kohler, S., Begelman, M. C. & Beckwith, K. Recollimation boundary layers in relativistic jets. *Mon. Not. Roy. Astron. Soc.* **422**, 2282–2290 (2012).

[29] Wykes, S., Hardcastle, M. J., Karakas, A. I. & Vink, J. S. Internal entrainment and the origin of jet-related broad-band emission in Centaurus A. *Mon. Not. Roy. Astron. Soc.* **447**, 1001–1013 (2015).

[30] Gopal-Krishna & Wiita, P. J. Extragalactic radio sources with hybrid morphology: implications for the Fanaroff-Riley dichotomy. *Astron. Astrophys.* **363**, 507–516 (2000).

[31] Keppens, R. *et al.* Parallel, grid-adaptive approaches for relativistic hydro and magnetohydrodynamics. *J. Comput. Phys.* **231**, 718 – 744 (2012). Special Issue: Computational Plasma PhysicsSpecial Issue: Computational Plasma Physics.

[32] Porth, O., Xia, C., Hendrix, T., Moschou, S. P. & Keppens, R. MPI-AMRVAC for Solar and Astrophysics. *Astrophys. J. Supp. Ser.* **214**, 4 (2014).

[33] Harten, A., Lax, P. D. & Van Leer, B. On upstream differencing and godunov-type schemes for hyperbolic conservation laws. In *Upwind and High-Resolution Schemes*, 53–79 (Springer, 1997).

[34] Sethian, J. A. & Smereka, P. Level set methods for fluid interfaces. *Ann. Rev. of Fluid Mech.* **35**, 341–372 (2003).

[35] Perucho, M. & Martí, J. M. A numerical simulation of the evolution and fate of a Fanaroff-Riley type I jet. The case of 3C 31. *Mon. Not. Roy. Astron. Soc.* **382**, 526–542 (2007).

[36] Lohner, R. An adaptive finite element scheme for transient problems in CFD. *Comp. Methods in Applied Mechan. and Eng.* **61**, 323–338 (1987).

Correspondence
Correspondence should be addressed to K.N.G. or S.S.K.

Acknowledgements
The authors acknowledge STFC grant ST/N000676/1. Simulations were performed on the STFC-funded DiRAC I UKMHD Science Consortia machine, hosted as part of and enabled through the ARC HPC resources and support team at the University of Leeds. We thank Dr Oliver Porth for insightful discussions of the intricacies of AMRVAC code.

Contributions
Both authors contributed to planning this research and the analysis of its results. All the simulations were carried out by KNG.

Competing financial interests
The authors declare no competing financial interests.

Model	$L_{j,44}$	Γ_0	θ_j	$\rho_{j,0}/\rho_{e,0}$	z_{RP}	x, y, z	t
U1	2	5	0.2	1	2.1	$1.2 \times 1.2 \times 4$	33
U2	2	5	0.2	64	2.1	$1.2 \times 1.2 \times 4$	33
C1	2	5	0.2	1.6×10^{-2}	2.3	$0.8 \times 0.8 \times 4$	33
C2	2	20	0.2	10^{-3}	2.3	$0.8 \times 0.8 \times 4$	33
C3	5	10	0.2	10^{-2}	6.4	$1.2 \times 1.2 \times 10$	65
C4	20	20	0.2	10^{-2}	30.0	$6.0 \times 6.0 \times 40$	150
C5	2	5	0.1	6.4×10^{-2}	2.2	$0.4 \times 0.4 \times 4$	13

Supplementary Table 1: **Simulation models.** The first column is the model name. For cases where the external gas is uniform it starts with letter U and for cases where it describes galactic corona with letter C. The second column is the jet power in units of 10^{44}erg s^{-1}. The third is the jet Lorentz factor at the centre of the nozzle. The fourth is the initial jet opening angle in radians. The fifth is the jet-external gas density ratio at the nozzle. The sixth is the distance of the reconfinement point from the origin in kpc. The seventh is the size of the 3D computational domain in kpc. The last column column gives the integration time of the 3D runs in kyr.

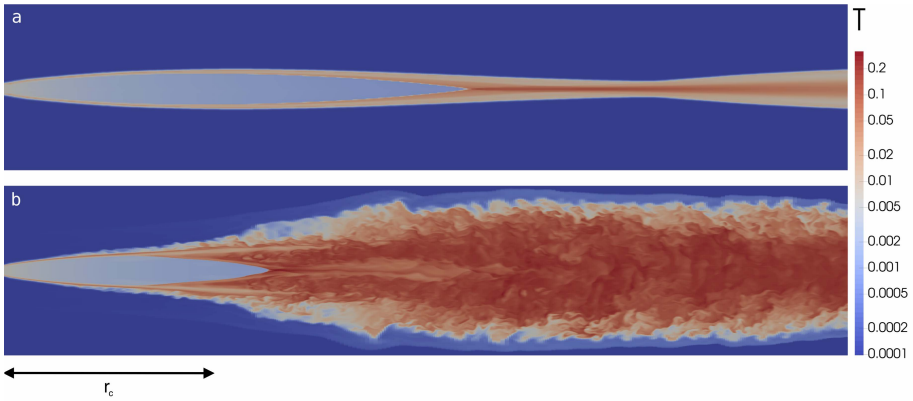

Supplementary Figure 1: **Temperature distribution in the xz-plane of the model C1**. The initial state is shown in panel a; and the final in panel b (t = 32.6 kyr). The sharp rise in temperature demonstrates the conversion of the kinetic energy into heat. The units are arbitrary as in Supplementary Figures 2 and 5 and 7.

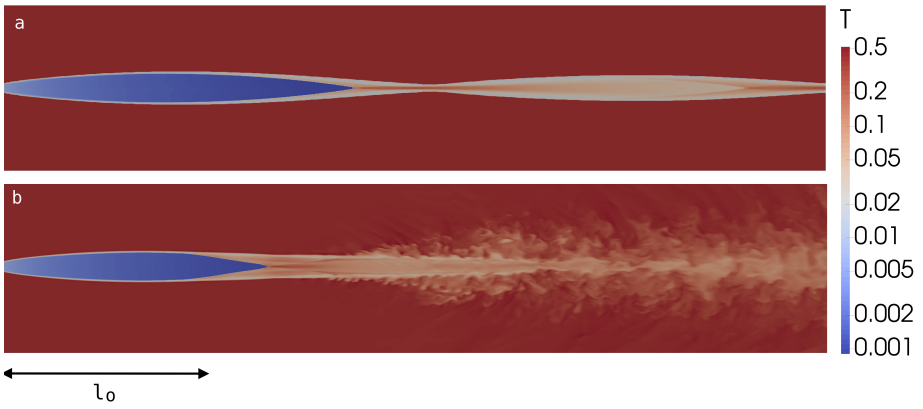

Supplementary Figure 2: **Temperature distribution in the xz-plane of the model U2.** The initial state is shown in panel a; and the end of the run in panel b (t = 32.6 kyr). In this model the external gas is lighter compared to the jet, thus representing the case of a jet reconfined by the thermal pressure of its radio lobe. Once the jet becomes unstable, its temperature rises but does not exceed that of the external medium.

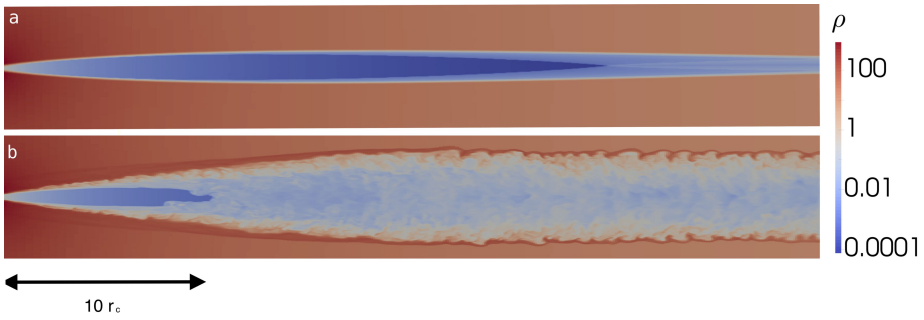

Supplementary Figure 3: **Density distribution in the xz-plane of the model C4**. The initial state is shown in panel a; and the state at the end of the run in panel b (t = 150 kyr). This jet is much more powerful compared to the C1 jet and reconfines well outside of the galactic core r_c. Nevertheless it shows the same behaviour: it develops instabilities and turns turbulent on the reconfinement scale.

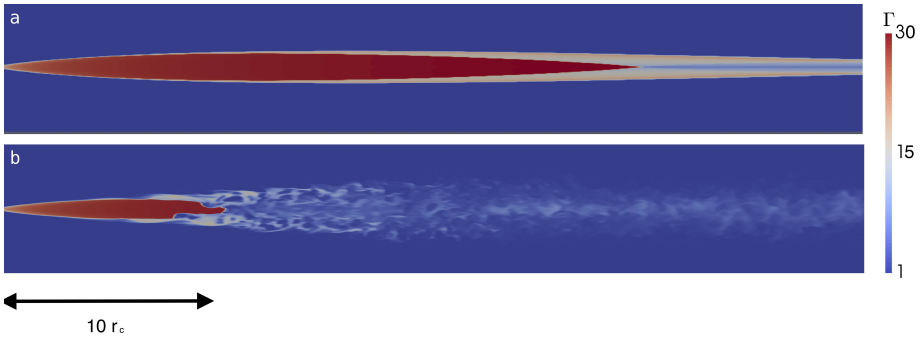

Supplementary Figure 4: **Lorentz factor distribution in the xz-plane of the model C4.** The initial state is shown in panel a; and at the end of the run in panel b (t = 150 kyr). The very high Lorentz factor of the jet does not prevent it from developing instabilities on the reconfinement scale.

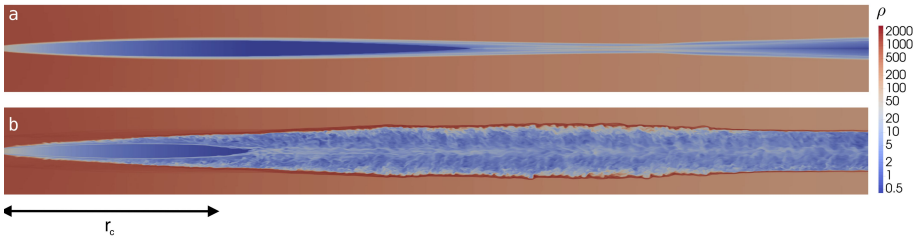

Supplementary Figure 5: **Density distribution in the xz-plane of the model C5.** The initial state is shown in panel a; and at the end of the run in panel b (t = 13 kyr), one light-crossing time of the computational domain along the jet axis. This jet has the same power as in the model C1 but its opening angle is smaller by a factor of two, θ_j = 0.1rad. Despite the smaller curvature of its streamlines the jet becomes unstable in a similar manner to the other runs.

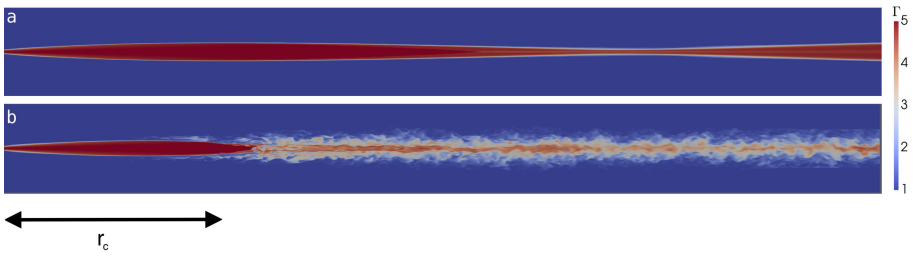

Supplementary Figure 6: **Lorentz factor distribution in the xz-plane of the model C5.** The initial state is shown in panel a; and at the end of the run at panel b ($t = 13$ kyr). Following the destabilisation at PR, the Lorentz factor drops in accordance with the other models. The spine-sheath structure of the jet is manifest as well.

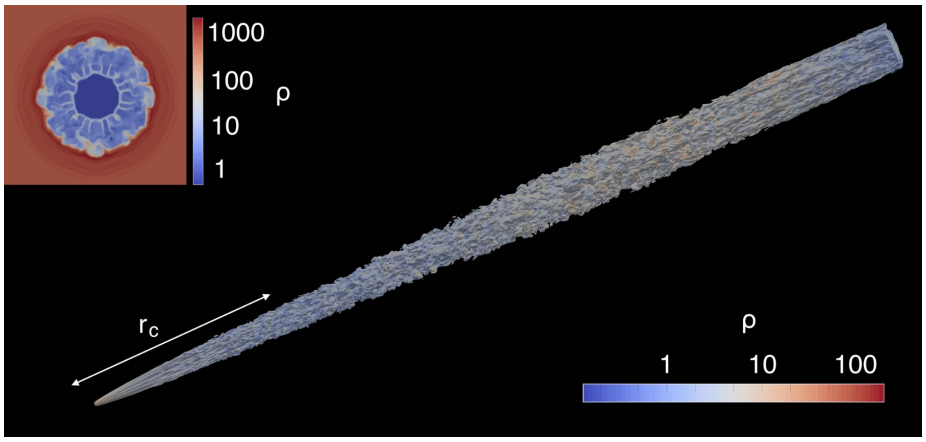

Supplementary Figure 7: **3D rendering of the model C5 at** $t = 13$ **kyr**. The main image shows the distribution of the rest mass density on the surface where the passive tracer $\tau = 0.5$. The insert in the top-left corner shows the density distribution across the jet at $z = r_c$. Like in the models with larger opening angle, this jet also develops stream-aligned structures characteristic of the centrifugal instability.